Silicon
https://doi.org/10.1007/s12633-024-03092-8

RESEARCH

Performers of Si_3N_4 Concentrations on Morphology and Electrical Behavior for New Quinary Fabrication PEO-CMC-PANI/GO@Si_3N_4 Nanocomposites for Electronic Devise and Gas Sensor Application

Rawaa A. Abdul-Nabi[1,2] · **Ehssan Al-Bermany**[1]

Received: 11 June 2024 / Accepted: 10 July 2024

Abstract
Gas sensors are critical topics, attracting scientists and industries for their ability to work in different environments for safety and environmental monitoring applications. The impact of various concentrations of silicon nitride ($Si_3N_{4[Y\%]}$) (Y = 0.2, 2.2, and 4.2%) compact with synthesis graphene oxide ($GO_{[0.8\%]}$) as ($GO_{[0.8\%]}$@$Si_3N_{4[Y\%]}$) hybrid nanomaterials loaded into newly ternary blend polyethylene oxide, carboxymethyl cellulose, and nano polyaniline ($PEO_{[60\%]}$-$CMC_{[30\%]}$ -$PANI_{[x\%]}$) to fabricated newly nanocomposites for nanochemical NO_2 gas sensor. Sol–gel and ultrasonic mixing methods were used to make nanocomposites, which were then dried out on glass slides using thermal evaporation to characterize the sensors. Images from field emission scanning electron microscopy (FESEM) and transmission electron microscopy (TEM) showed that the shape and porosity of the surface changed a lot. These changes, along with the attachment of nanomaterials, are key to how well it can sense gases. The Fourier-transform infrared spectroscopy (FTIR) spectra showed that the sample components had strong physical and network interactions. X-ray diffraction (XRD) indicated a semi-crystalline behavior in all samples. Dialectical constant and loss were reduced, whereas AC electrical conductivity improved with the increase in the content of Si3N4. The gas sensor ran at three temperatures (RT, 100 °C, and 200 °C). All of the nanofilm sensors behaved like p-type semiconductors, and when the oxidized gas NO_2 was turned on, the electrical resistance went down. The best sensitivity to NO_2 was (6.89%) at RT, with a response time of (16 s) and a recovery time of (19 s) for a loading ratio of 3 wt.% hybrid nanomaterials. The study provides an excellent nanochemical gas sensor for NO_2 gas for manufacturing applications.

Keywords Electrical properties · Sensor · Nitrogen oxides · Response time · Silicon nitride · Graphene

1 Introduction

The modern period of high technology and sophisticated manufacturing has resulted in unbelievable growth and a remarkable increase in standards of living. Nevertheless, this has been accompanied by various severe environmental issues, including the discharge of various chemical contaminants into the atmosphere, which has led to global ecological problems, for instance, the effect of greenhouse, depletion of ozone, sick house syndrome, and acid rain [1]. Life's safety is of utmost significance since our environment consists of main occupants such as plants, humans, animals, etc. Different amounts of gases, such as volatile organic compounds (VOCs), NO, NH, SO, HCl, CO, fluorocarbon, etc., are present in the air around us from industry, cars, and homes. These gases may harm the health of humans and pollutants of the atmosphere and be substantial to medical and industrial developments. Consequently, detecting the presence of gas is crucial because it is essential to human life and plants and animals in our environment. Due to the requirement for accurate and immediate measurements of the concentration of a specific gas, conventional detection techniques, which result in devices that emit an auditory alert to alert people to dangerous or toxic gas leaks, are not exceptionally dependable [2].

A sensor is an electronic device. It detects and converts information or stimuli into electrical signals [3]. An

✉ Ehssan Al-Bermany
ehssan@uobabylon.edu.iq

[1] Department of Physics, The Faculty of Education for Pure Science, University of Babylon, Babylon Govermant, Hilah 50001, Iraq

[2] Electrical Engineering Techniques Department, Technical College Al-Mussaib, AL-Furat AL-Awssat Technical University, Al-Mussaib, Babylon, Iraq

Published online: 27 July 2024

alternative definition of a sensor is a device detecting and sensing various physical stimuli, for instance, pressure, heat, sound, magnetism, light, etc., and converts them into electrical signals [4]. Sensors can be categorized into different groups based on the specific physical quantity or analyte being measured, as shown in Fig. 1. The categories encompass energy source, physical contact, comparability, analog and digital, signal detection sensors [5, 6]. The list of the specifics for each classification is as follows.

One kind of sensor that can examine our surroundings is the chemical sensor, which examines our surroundings by identifying the presence and relative quantities of different chemicals. Humans possess five sensory organs bestowed upon them by a that God has given us. These sensory organs enable us to perceive visual, auditory, olfactory, and gustatory sensations. Chemical sensors may be synthetic olfactory or gustatory organs [4].

The International Union of Pure and Applied Chemistry (IUPAC) defines a gas sensor as follows: a chemical sensor is an electrical device that transfers chemical information to an analytically usable signal. The chemical information, such as the single sample component concentration or the overall configuration analysis, might result from a physical feature or analytic chemical reaction of the system under investigation. Sensors are generally made of two main elements: a receptor and a transducer. The receptor presents the energy that transforms from the chemical information, whereas the transducer converts this energy into a typically electrical, practical, and analytical signal [7]. The receptor component is based on many principles, including physical, in which no chemical reactions occur. At the same time, a chemical reaction takes place here. When the analyte reacts chemically with the receptor, it produces an analytical signal. Biochemical: In this case, the analytical signal originates from the biochemical process, including but not limited to immunological sensors and microbial potentiometric sensors. This kind of sensor is called a biosensor [7, 8].

Gas sensors are very significant chemical sensors. The gas sensor has various essential parameters that need attention to enhance the sensor's performance. These parameters include sensitivity, selectivity, response and recovery time, stability, detection limit, linearity, hysteresis, and detection limit. Currently, no sensor exhibits complete selectivity for a single gas. However, ongoing research aims to produce sensors that can achieve optimal operational efficiency [9, 10]. The gas sensor device can detect the presence and quantity of a specific gas molecule. These sensors may be used for controls on air quality, the prevention of hazards, the inspection of food, and the monitoring of human health. It can get a warning from these gas sensors if the concentration of a particular gas exceeds the range of permissible, acceptable levels [10]. Gas sensors are fabricated using diverse materials based on the application's requirements. Every type of gas sensor can detect the existence of a particular chemical molecule, which in turn produces a distinct response from the sensor. Sensors were categorized into various types

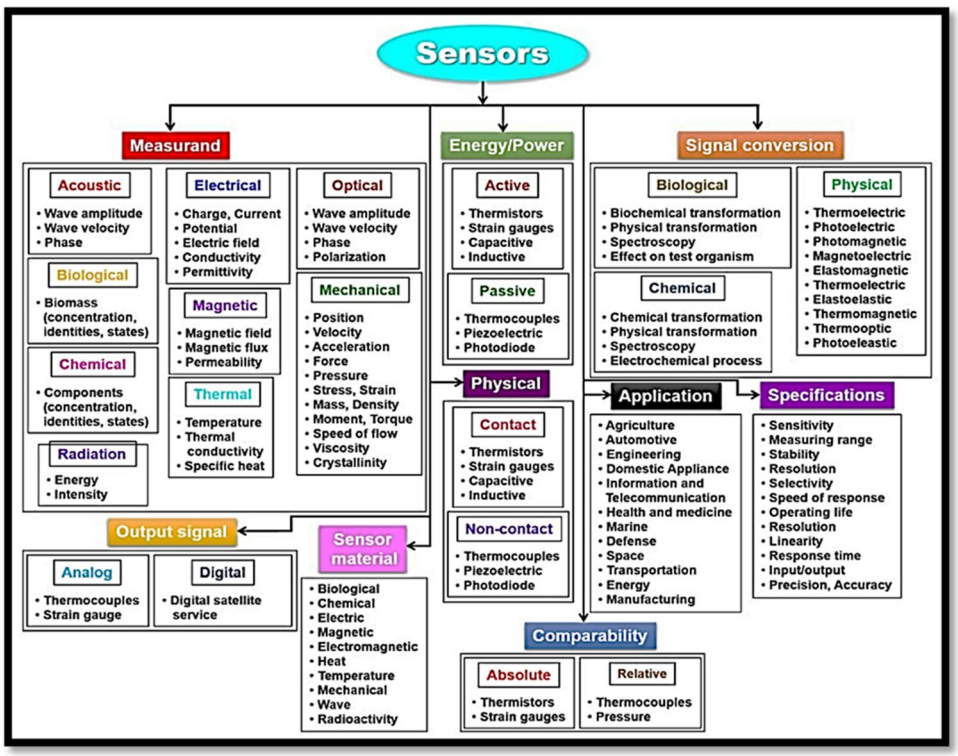

Fig. 1 Sensors classification according to material, energy, physical contact, comparability, specification, signal conversion or output, and applications (Reproduced from White et al. Ref [5, 6])

according to information in the kinds of literature [11, 12] into two different groups based on their underlying functioning principle, as shown in Fig. 2.

Polyethylene oxide (PEO) is a large molecular weight polymer recognized for its ability to dissolve in many substances, compatibility with living organisms, and wide range of applications. It serves as a vital component in medicinal, pharmacological, industrial, and environmental contexts [13]. The capacity to create hydrogels and their lack of toxicity renders them highly valuable in drug delivery systems, medical devices, and tissue engineering. The vast range of applications for PEO underscores its significance in multiple domains, including the improvement of product formulations and the advancement of biomedical technologies [14]. The PEO molecule can be represented by the generic formula $(CH_2CH_2O)_n$, where "n" denotes the quantity of repeating ethylene oxide units. PEO commonly denotes polymers with larger molecular weights (more than 20,000 g/mol), while PEG generally refers to polymers with lower molecular weights. Nevertheless, the names are occasionally employed interchangeably [15].

Carboxymethyl cellulose (CMC) is a multifunctional and extensively employed cellulose derivative. Due to its notable characteristics, such as its ability to dissolve in water, its thickness, and its compatibility with living organisms, it is a crucial component in the pharmaceutical, cosmetics, food, and industrial [16]. Carboxymethyl cellulose (CMC) is a very efficient thickening agent, stabilizer, emulsifier, and film-forming agent, improving various products' texture, stability, and overall performance. The extensive uses and lack of toxicity highlight its significance in consumer and industrial goods. CMC is a cellulose derivative, a naturally occurring polymer [17]. The substance is created by chemically altering cellulose by adding carboxymethyl groups

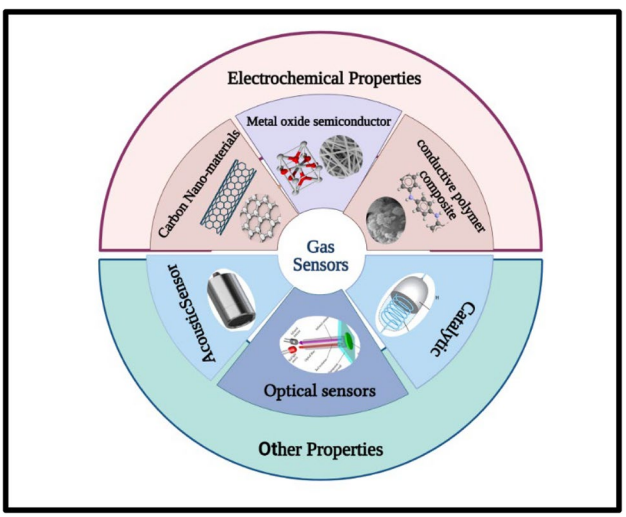

Fig. 2 Different types of sensors used in gas sensing

(-CH_2-COOH) to the cellulose structure [18]. CMC exhibits its excellent water solubility, resulting in the formation of thick solutions. The solubility and viscosity of the polymer are contingent upon the degree of substitution (DS) and the molecular weight of the polymer. Carboxymethyl cellulose (CMC) is characterized by its non-toxicity and biocompatibility, rendering it very appropriate for application in the fields of food, medicines, and cosmetics [19].

At early 1980s [20], conducting polymers, including polypyrrole (PPy), polythiophene (PTh), polyaniline (PANI), and its derivatives. Among them, polyaniline (PANI) has gained significant interest recently due to its numerous advantageous characteristics to be applied as the active layers of gas sensors. Additionally, its ability to strongly absorb visible light, relatively high electrical conductivity, intriguing redox properties, lower density compared to metals, energy storage capabilities, straightforward synthesis process, moderate conductivity, suitable environmental and thermal stability, and low cost. Regarding its chemical composition, PANI combines oxidized quinoid diamine repeating in addition to reduced benzenoid diamine and units. Depending on the value of reduced benzenoid diamine, the oxidation state of PANI may be determined [21]. PANI chemical structure is a vinyl ring with an N–H Group. Each repetition unit has three benzene rings, separated by (−NH) amine groups and one quinoid ring surrounding imine groups (−N=). Nitrogen creates double bonds with the quinoid ring. In the ring, there are two carbon atom pairs and four π-electrons. The polymer's macroscopic structure is a complex network of long chains of repeating units [22].

Graphene nanomaterials have recently been found to have sensing applications [23, 24]. This is because of graphene's numerous remarkable properties, including its high carrier mobility, low electrical noise, large surface area, ballistic conductivity, and excellent thermal stability at room temperature resulting from their unique 2D honeycomb lattice [25, 26]. The fact that gas molecules adsorb strongly to graphene's electrical characteristics is the most crucial reason for its potential as a nanomaterial for gas sensing. Regarding sensitivity, graphene is unrivaled; the planar structure of graphene, simplicity of processing, and other possible benefits are also shown by graphene [27, 28].

Novoselov's group announced in 2007 the first gas sensor based-graphene [25], demonstrating that micrometer-sized graphene sensors can detect individual gas molecules. It can detach or adhere to the surface of graphene nanosheets. They demonstrated that the adsorption of the molecules modified the local carrier concentration in graphene by one electron. It assists in a gradual difference in resistance. The change showed the ability of the gas to act as an electron acceptor, for example, iodine, NO_2, and H_2O, or an electron donor, for instance, ethanol, CO, and NH_3 [24, 29]. The critical performance-enhancing approaches in sensors-based graphene

have been discovered to be hybridization, functionalization, and doping. Graphene oxide (GO) is a carbon nanosheet that has recently evolved and is commonly recognized to be connected to graphene [30]. GO is a single-atomic layer material with similar properties to graphene but an extra set of functional groups on its surface [31]. These groups have converted GO to hydrophilic states that make them simple to disperse in water and various solvents. In addition, they have a wide surface area that makes them suitable for deposition. In particular, GO can strongly interact with various small molecules and macromolecules [32].

Silicon nitride (Si_3N_4) is a ceramic material with exceptional mechanical, thermal, and chemical characteristics, making it highly suitable for demanding applications. It is extensively utilized in applications requiring superior strength, thermal stability, and the ability to withstand wear and corrosion [33]. The versatility of Si_3N_4 makes it indispensable in several industries like mechanical engineering, electronics, automotive, aerospace, and medical. Due to its durability and performance properties, it is highly valued as a material for vital components and innovative technologies [34]. Si_3N_4 comprises silicon and nitrogen atoms bonded in a robust covalent structure. It possesses a high electrical resistance and functions as an electrical insulator. Si_3N_4 is unreactive, impervious to oxidation, and immune to corrosion caused by most acids and alkalis [35].

Researchers have investigated chemical or physical methods to improve graphene's gas-sensing capabilities [36–39]. Over the last few years, many reviews dealing with polymeric materials in gas sensing technology have been published in this article, are reviewed. The present paper highlights gas sensors based on the impact loading ratio of Si_3N_4 nanoparticles with GO on characterizations of turnery blended biocompatible and conducting polymers as nanocomposites for AC electrical peripeties and toxic gas sensors.

2 The Experimental Part

2.1 Materials

PEO is a white color that has a (100 000) $g.mol^{-1}$ molecular weight (Mw), crystal-granular with chemical formula (O-CH_2-CH_2)n, produced by Sigma-Aldrich Company, the UK. CMC has Mw of (700,000) g.mol-1, with viscosity (5000) min, linear and chemical formula (C_6H_9NO) n, white or yellowish color, powder, supplied from Cheng Du Micxy Chemical Co. Ltd., China. PANI Nano polymer with nanoparticle size of (20 nm), a molecular weight of (150,000) g/mol, and chemical formula (C_6H_7N)n dark/light green/black powder or paste color, were purchased from Panichem Company, LTD, Korea. Silicon nitride nanoparticles with nanopowders size between (15–30) nm and a molecular weight of (140.28) g/mol, grey-white color and purity of (99%), a melting point of (1900 °C), and cubic crystallographic form, which was supplied from Telligent Materials Pvt. Ltd., India. Synthesized GO used a modified Hummer process [33] following our group's procedure with full characterizations from a previous publication [40].

2.2 Formation and Mixing of Samples

Samples were fabricated using the flowing procedure, as shown in Table 1 and Fig. 3.

1. All polymers were dissolved using distilled water (DW) independently, briefly, 9 gm dissolved in 150 ml. It was dissolved by mixing for 24 h at an ambient temperature to ensure complete dissolution, as presented in step 1 in Fig. 3.

   Independently, nanomaterials were dispersed in DW with gentle sonication for better dispersion before loaded and mixing. Briefly, 0.5 wt. % of GO was dispersed in DW for 72 h with mixing and sonication for 10 min in a sonication bath for each 1 h of mixing time of the first 3 h of combining to become 30 min as total, the only missing using stirrers to achieve nanosheet exfoliation, and Si_3N_4 with the same ratio of GO was also distributed in DW for 24 h with the assist of bath sonication for 30 mints separated as 1o mint each time as process of GO. Si_3N_4-DW were loaded with different loading ratios (Y=0.2, 2.2, and 4.2)%. Each concentration was mixed with dispersed $GO_{[0.8\%]}$-DW to fabricated ($GO_{[0.8\%]}$@ $Si_3N_{4[Y\%]}$) hybrid nanomaterials with three different ratios (1, 3, and 5) %, as presented in step 1 in Figure 3.
2. To prepare the first binary blended polymer, PEO and CMC polymers mixed with fixed ratios of $PEO_{[60\%]}$-$CMC_{[30\%]}$ in proportions in (60:30) wt.% to fabricate (B). It was mixed for 72 h at an ambient temperature to ensure complete homogeneity, as in step 2 in Fig. 3.

Table 1 The percentages of fabricated blend polymers and their nanocomposites

Sample ID	Concentration wt. %			
	PEO 100 K	CMC	PANI	GO: Si_3N_4
PEO	100	-	-	-
CMC	-	100	-	-
PANI	-	-	100	-
B	60	30	10	-
NC1	60	30	9	0.8: 0.2 = 1
NC2	60	30	7	0.8: 2.2 = 2
NC3	60	30	5	0.8: 4.2 = 3

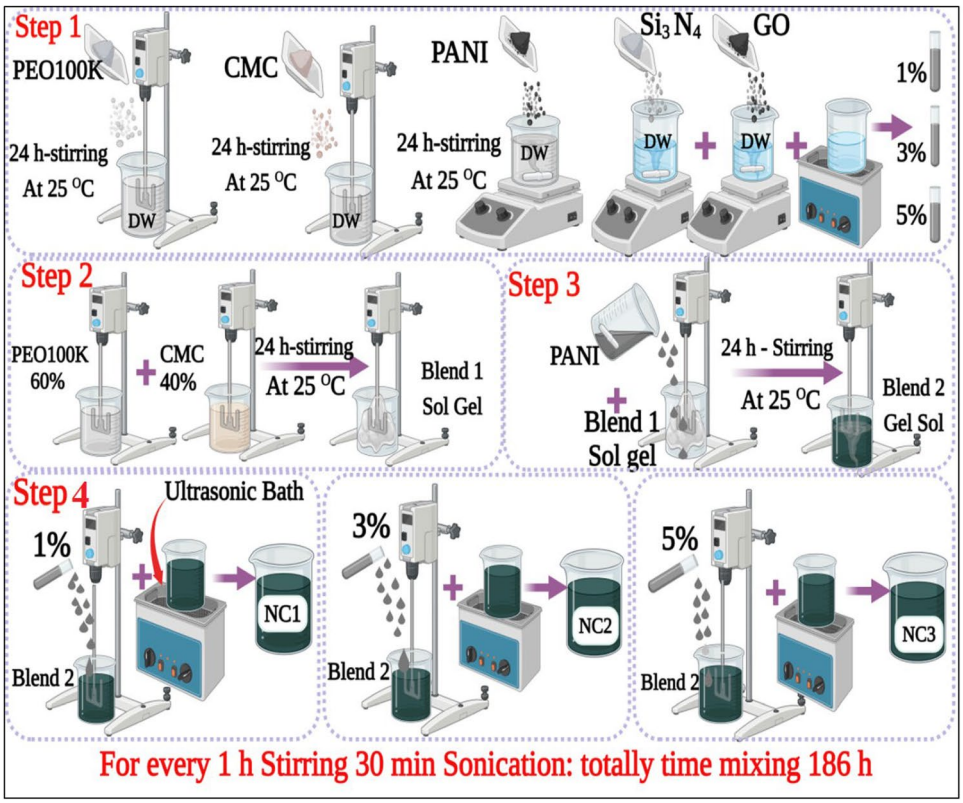

Fig. 3 Schematic of the experimental process in this study

3. Different ratios of nano $PANI_X$ (X = 10, 9, 7, and 5) wt.% were used to fabricate the ternary blend polymers $PEO_{[60\%]}$-$CMC_{[30\%]}$-nano $PANI_{[x\%]}$,, as presented in step 3 in Fig. 3.
4. Using different loading ratios (1, 3, and 5) % of ($GO_{[0.8\%]}$@$Si_3N_{4[Y\%]}$) hybrid nanomaterials into the ternary blended polymers in step 2 to fabricate novel quinary $PEO_{[60\%]}$-$CMC_{[30\%]}$-nano $PANI_{[x\%]}$/$GO_{[0.8\%]}$@$Si_3N_{4[Y\%]}$ nanocomposites, as shown in Table 1. The nanocomposites were mixed for 7 days. It was spread with the assistance of sonication using an ultrasonic bath during the mixing process at a rate of 1 h of mixing, interspersed with 30 min of sonication in total to obtain good homogeneity, as shown in step 4 in Fig. 3.

The head mechanical mixer purchased by the Kama-type was used to fabricate all the samples, as revealed in Fig. 3.

2.3 Characterizations

Table 2 summarizes the characterizations employed in this study.

3 Results and Discussion

3.1 Morphological and Structure Properties

FESEM was utilized to investigate the surface, morphology, and distribution of GO@Si_3N_4 and within ternary blended polymers (PEO-CMC-PANI) and their nanocomposites. Figure 4 demonstrates two FESEM image magnifications, micro-size and nano-size (inset images), for each pure polymer, nanomaterials, ternary blend polymers, and novel quinary $PEO_{[60\%]}$-$CMC_{[30\%]}$-nano $PANI_{[x\%]}$/$GO_{[0.8\%]}$@$Si_3N_{4[Y\%]}$

Table 2 The details of used characterizations

Characterization	Type	Details	Company
FTIR	Spectrum IR-10.6.2	4000–400 cm^{-1}	PerkinElmer, the USA
X-ray	AERIS	40 kV,7.5 Ma, Cu tube target	Malvern Pan Analytical, Netherlands
FESEM	Inspect F50	30 kV, 120μA	FEI Company, Netherlands
STEM II	Nano NanoSEM 450	12 kV, 120μA	FEI Company, Netherlands
AC electrical	(3532–50, Hi TESTER)	LCR meter	Hioki, Japan

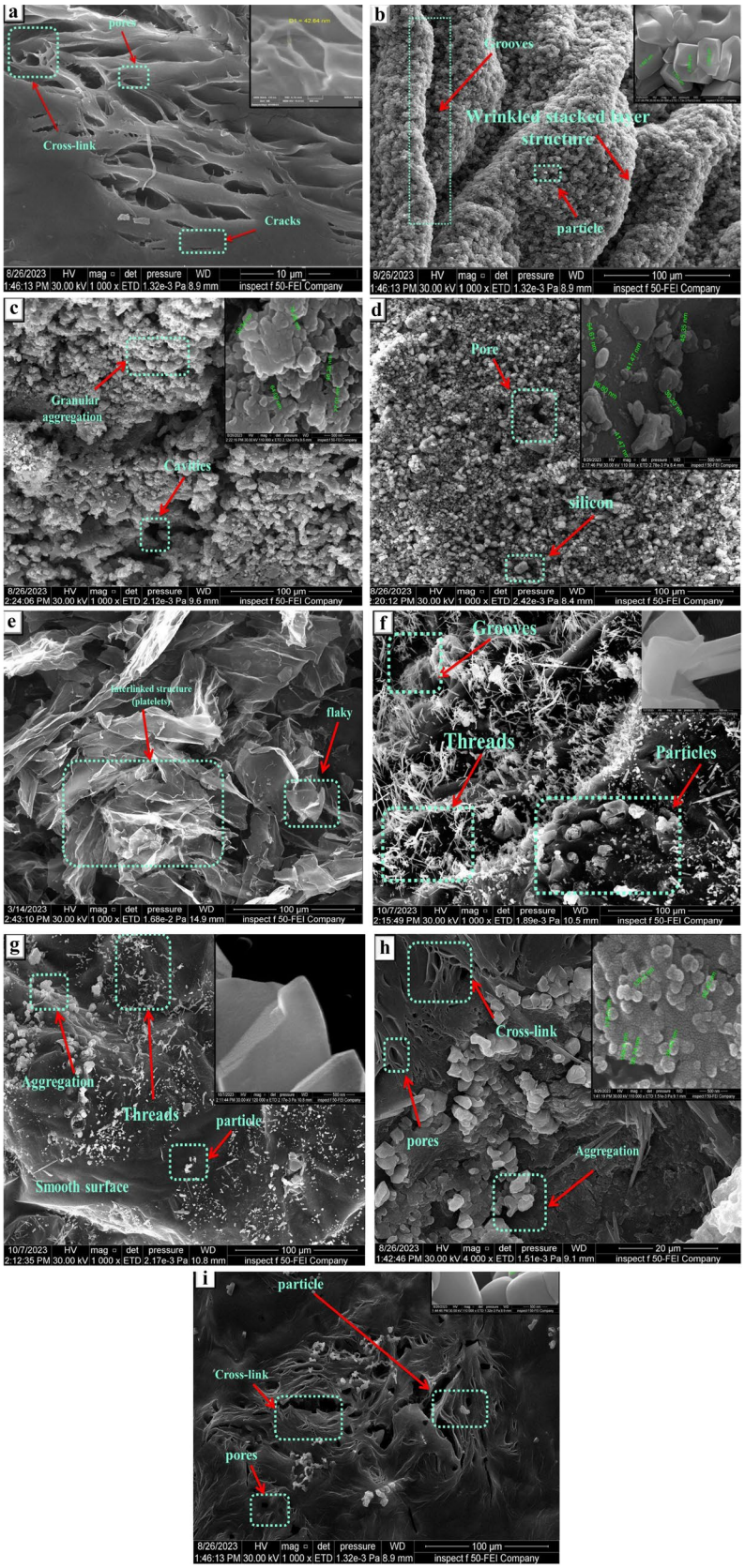

Fig. 4 FESEM images with micron size and nanosize for (**a**) pure PEO, (**b**) pure CMC, (**c**) pure PANI, (**d**) Si_3N_4, (**e**) GO, (**f**) ternary blended polymers B, (**g**) NC1, (**h**) NC2, and (**i**) NC3

nanocomposites with different concentrations of (GO@Si_3N_4). The surface morphology of the pure PEO is shown in (Fig. 4a); it was a smooth surface with evident cavities and cracks [41] and displayed a highly porous structure responsible for high ionic conductivity. The solvent removal and retention ability could be associated with pores in the polymer microstructure [42].

The CMC is also shown in Fig. 4 (b), a rough, uneven, layered, and wrinkled zigzag surface morphology and elongated grooves or channels along the film [43]. Nano PANI (4c) FESEM image shows a rough structure, deep cavities, and agglomerated and macro-granular morphology [44] formed by the small globular aggregation in the structures. This could related to the rise in the inner interactions of polymer chains and separated cauliflower aggregation structures [45]. The SEM micrograph of pure Si_3N_4 (4d) shows relatively uniformly distributed silicon (Si) in the remark area [46], having minimal gaps or areas exhibiting varying silicon concentrations. Figure 4e illustrates the flaky morphology of GO that displays a nanosheet-like porous within the 2D-dimensional and interconnected structure that formed through the exfoliation process and restacking [47].

When polymers are mixed, the surface of the ternary blend polymers is significantly changed. It presented a rough structure with some particles of different sizes [48], cavities, and threads or nanofibers belonging to the nano polyaniline polymer, as shown in Fig. 4f. In Fig. 4g, 1% of nanomaterial loaded into quinary $PEO_{[60\%]}$-$CMC_{[30\%]}$-nano $PANI_{[9\%]}$/$GO_{[0.8\%]}$@$Si3N4_{[0.02\%]}$ nanocomposites exposed some entangled thread similar network of PEO, CMC, PANI, and nanomaterial, became uniformly distributed.

The effect of GO and Si_3N_4 appeared on the polymers and became more bonded, and the surface was more like smoother [13], especially after increasing the concentration of Si_3N_4. The pores and cavities disappear and show particles of different sizes and agglomerates. When increasing the percentage of Si_3N_4 in the sample to 3%, as shown in Fig. 4h, more homogeneous materials in some areas and a smooth surface are noticed. The polymers are linked with each other in a way that resembles arms, interspersed with some pores; these pores reveal the creation of a porous compact structure as a result of the nanograins or nanofibers contained in polyaniline [49]. In addition, increasing the GO ratio showed some aggregations [50]. The behavior of the presence of cavities and pores remains the same.

Increasing the nanomaterials to 5% associated with the presentation of the porous structure resulting from the nanograins and nanofibers of PANI increased, and the linking became more extraordinary due to the excellent interaction associated with interlocated nanomaterials into the matrix and reduction on the surface that occurred because of continuous mixing between the components. In addition, the surface became smoother in other parts, and a radical and strong change happened in the sample's surface, as shown in Fig. 4i. This might indicate a growth as a homogenous process [50].

The internal structure of the sample and the arrangement of atoms within it were examined by applying TEM, which provides high-resolution transmitted electron imaging of two samples, GO@Si_3N_4 and NC3 nanocomposites, as presented in Fig. 5. In Fig. 5a and b, TEM micrographs of GO@Si_3N_4. GO showed fine homogeneous dispersion of single multi nanosheets of GO, and some nanosheets were aggregated in another place due to the physical attraction between them. This behavior was also observed in Si_3N_4 nanomaterials, which presented a spherical-like amorphous [51]. It revealed good dispersion in the samples; others were bonded with GO, as clearly presented in Fig. 5 b. Interestingly, Si_3N_4 presented surrounded by the GO nanosheets as core and shell in some places that were uniformly distributed [46]. The link appears in most regions between GO and Si_3N_4 nanoparticles, in addition to flat and morphology aggregated sheets of GO, seems to be a flake such as a film that can propose a large specific surface area [50].

The TEM micrographs of NC3, presented in Fig. 5c, d, and e, depict the homogeneous dispersion of the tertiary polymer blend particles that sounded GO@Si_3N_4 nanomaterials and the bonded appear in most regions between nanomaterials. Additionally, nano PANI, Si_3N_4, and GO are dispersed on the surface, and the polyaniline is presented as a rod-like structure in agreement with literature [52], the Si_3N_4 nanoparticles are spherical-like amorphous [51]. The flat structure of GO is a flake, such as a film, that can provide a large specific surface area and is beneficial for the loading of nanomaterials. Core–shell appears in some places where the surfaces of the GO@Si_3N_4 are coated or surrounded by a few tertiary polymer blend [53].

Figure 6 displays the FIR spectra of the blended polymers and their nanocomposites after doping (GO@Si_3N_4) nanomaterials in the ternary blended polymers. Ternary blended polymer (B) revealed several prominent functional group peaks at 3346, 2890, 1636, 1351, 1258, 1088, and 948 cm^{-1}. The presence of several hydroxyl and carboxyl groups in PEO and CMC led to the fabrication of strong hydrogen bonds, which can be identified by the O–H stretching vibration exhibited by these bands [48] and Si_3N_4 and/or N-JH stretch vibration in PANI [45], C-H stretching vibration, stretching C = C of quinoid ring (N = Q = N) [54], C-H bending, C–O–C stretching vibrations [55], C-O and other reported C-H in the hydrogel networks [56], respectively.

The functional peaks that related to PEO presented at 1351 and 948 cm^{-1} correlated to the CH_2 asymmetric wagging band [57] and contributed to the rocking vibration C–H absorption peak in the methylene group in the ternary blended polymer (B) [58]. A single peak (1258 cm^{-1}) associated with the CH bending mode also appears with

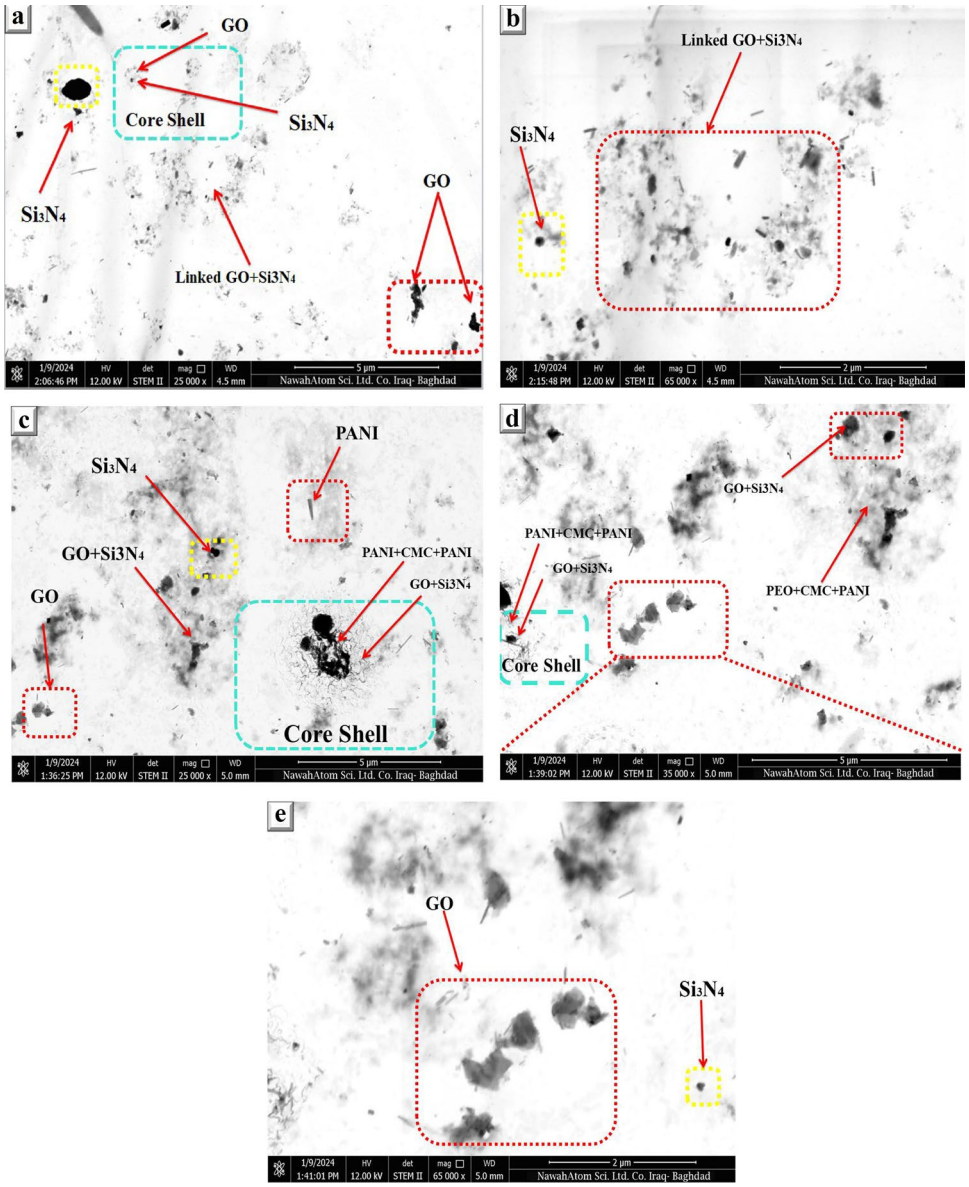

Fig. 5 TEM images of (**a** and **b**) GO@Si_3N_4 and (**c**, **d**, and **e**) NC3

a weak intensity related to PEO [59]. The most functional peaks competition the contained polymer peaks within the spectrum of ternary blended polymer (B). The results of the spectrum of quinary nanocomposites (NCs) presented the main beaks of the ternary blended polymer (B) spectrum. The exact position peaks at 3346, 1636, 1351, and 1088 cm^{-1}. At the same time, a clear peak was presented at 696 cm^{-1}, which could be associated with the Si–H bond [60]. It became clearly presented by increasing the concentration of Si_3N_4 In the matrix.

All samples generally showed strong absorption peaks at 3346, 1636, 1088, and 696 cm^{-1} as hydrogen interactions between ternary blended polymer (B) and nanomaterials. The contribution of the binary nanomaterial in nanocomposites appeared, which is responsible for the decrease in the intensity of most peaks. This is connected with creating the network among GO and Si_3N_4 nonmaterial and polymers, which strongly agrees with other findings [61]. Structural features of the blended polymer were not affected after the fabrication of the nanocomposites in agreement with another report [62]. The FTIR spectra characteristic of vibration bands formed in ternary blended polymers and quinary nanocomposites are displayed in Table (1S) in the (SI).

Figure 7 presents the XRD patterns for the ternary blended polymers (B) and their nanocomposites (NCs). The XRD pattern of polymers blend demonstrations four sharp peaks at ($2\Theta = 18.4°$, 22.7°, 30.8°, 44.7°) and other small intense peaks or features at ($2\Theta = 14.3°$, 25.4°, 26.2°, 30.8°, 34.6°, 35.5°, 38.8°, 44.7°, 55.8° and 74°) attributed to the characteristic peaks of all the matrix components PEO, CMC, PANI polymers [63]. The XRD pattern of ternary blended polymers (B) revealed the semi-crystalline

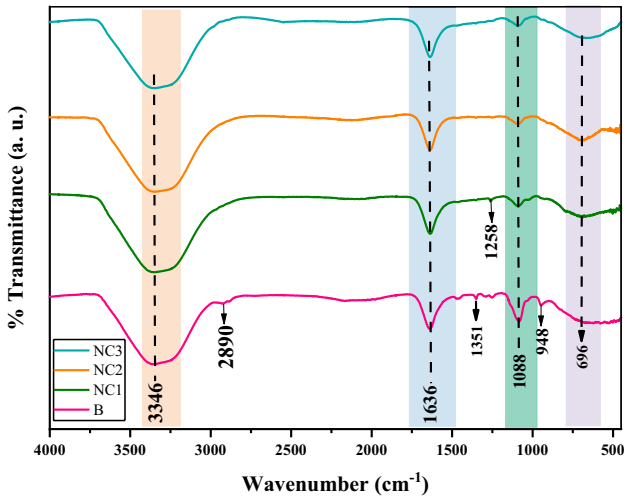

Fig. 6 FTIR spectrum for ternary blended polymer (B) and quinary nanocomposites (NCs)

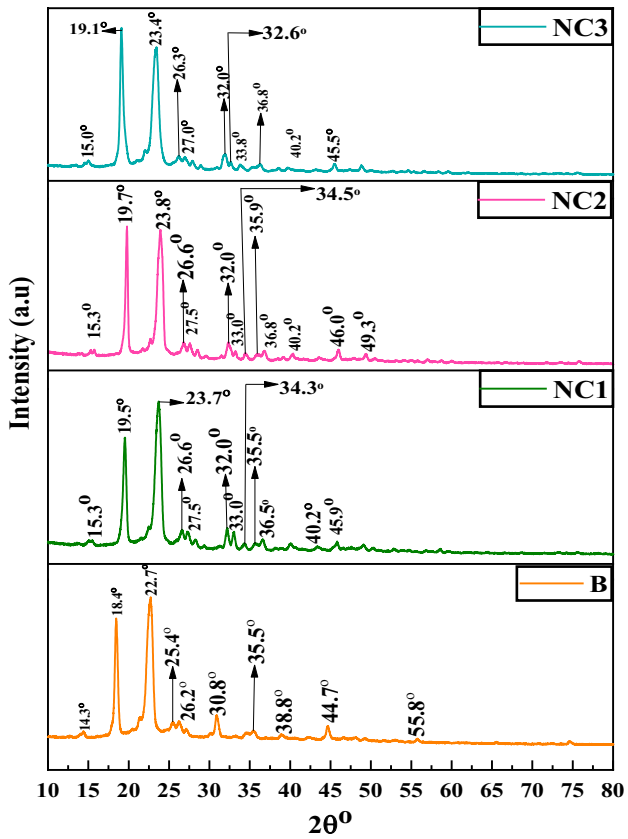

Fig. 7 XRD patterns with diffraction angle 2θ° for blend polymer B and their nanocomposites NC1, NC2, and NC3

nature of the polymer matrix due to the presence of the semi-crystalline structure of the PEO polymer. Where the main peaks at 18.4° and 22.7° are linked to PEO [13]. CMC semi-crystalize peak exhibited at 22.3° [64] overlapped with PEO peaks, whereas PANI revealed other small peaks [45].

The XRD patterns of the blend filled with the contributed of ($GO@Si_3N_4$) nanomaterials at different ratios (1, 3, and 5 wt. %) revealed redaction of the peak intensity with the adding and raising of (Si_3N_4) nanoparticles ratio. Moreover, the peaks revealed slight shifting in most of the peaks from their original positions. Specifically, NC1 revealed a sign of GO in 11.1° and 40.02° [65] and all other XRD diffraction peaks might be indexed to the Si_3N_4, a hexagonal structure matched (JCPDS Card no. 41–0360), and other reports [33].

In addition, the obtained XRD results proved the strong interaction and good distribution of the ($GO@Si_3N_4$) nanoparticles and the matrix blend, as demonstrated by FT-IR results and literature [55, 66]. Most peaks were shifted, and the intensity at around 19 increased to become higher compared with other peaks and blended samples; moreover, the dissolution of ($GO@Si_3N_4$) nanoparticles within the structure of the PEO-CMC-PANI polymer blend.

3.2 Dialectical Properties and A.C Electrical Conductivity

The dielectric constant of the ternary polymer mixture (B) and its nanocomposite doped were considered at room temperature within the range of (100 Hz to 5 MHz) frequency. The results are exposed in Fig. 8. Its dependency was computed by applying Eq. (1S) in (SI), as depicted in Fig. 8 (a). It exhibited a decrease for all samples as the frequency increased. At lower frequencies, the results of all samples were high, and as the frequency raised, it substantially reduced. When the dipoles are arbitrarily oriented in response to the external electric field, where the external electric field causes them to align parallel to it, creating an electric field that opposes the initial electric field, it reduces the strength of the initial electric field, enhancing the composite's dielectric constant. As the frequency rose, the value of the dielectric constant of the samples was reduced. This could relate to stating that at low frequencies, the duration of each cycle is long enough for the dipoles to reorganize and orient the molecules in a way that aligns them with the electric field. At high frequencies, the period was short and less than the period needed from the molecules to rearrange themselves in the external electric field direction, and also due to the difference in the phases of the base material and the support materials (micro-particles and nanoparticles), which results in interfacial polarization, which led to improving the results of the dielectric constant. In addition, the polarization resulting from the electrodes has a close relationship with the formation of the charge of the sample present between the two electrodes, the distances of the sample, and the composition. The dielectric constant value could also be impacted strongly by the ionic and

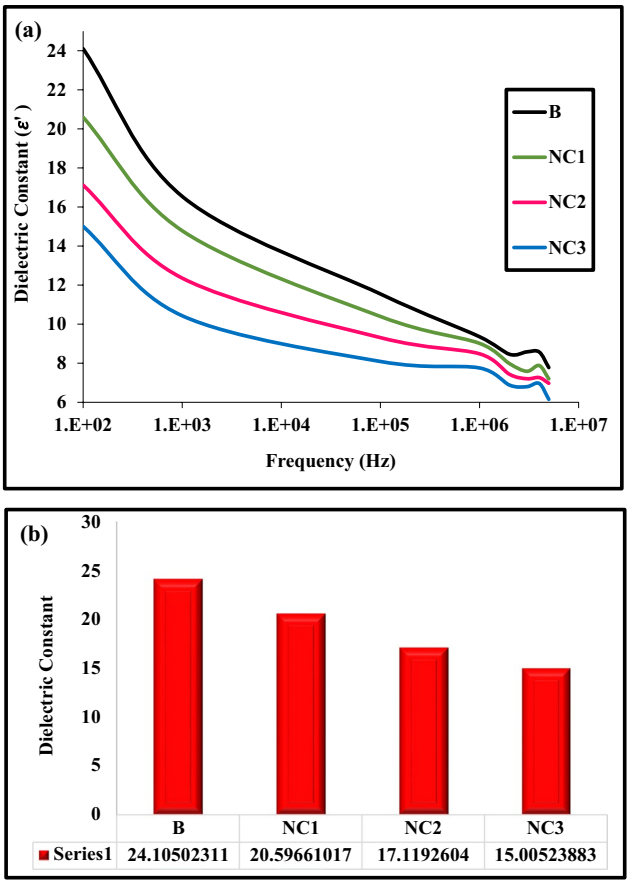

Fig. 8 The dielectric constant variation with (**a**) frequency and (**b**) impact of (GO@Si_3N_4) nanomaterials in nanocomposites (NCs) at 100 Hz

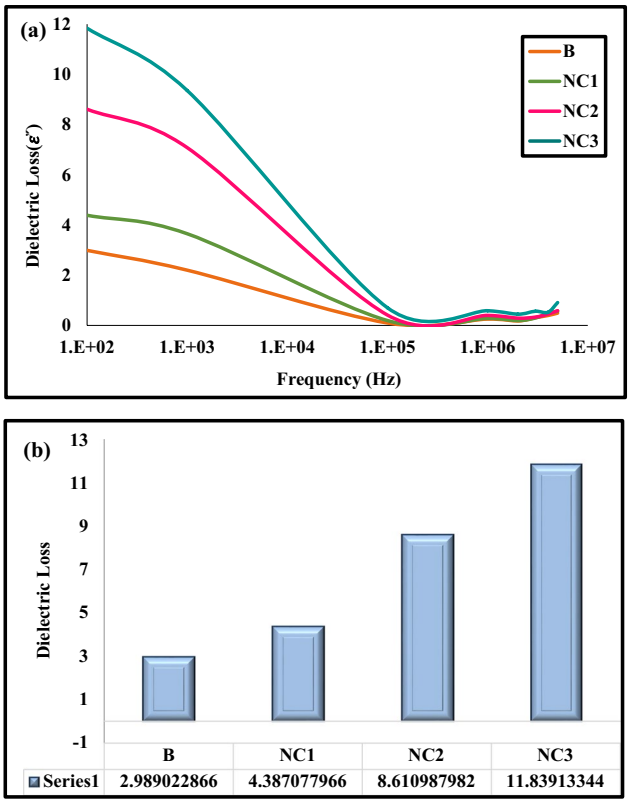

Fig. 9 Signifies Dielectric loss variation with (**a**) frequency and (**b**) impact of (GO@Si_3N_4) nanomaterials in nanocomposite at 100 Hz

electronic polarization that could follow the rotation of the applied external electric field, reducing polarization. Hence, the dielectric constant decreased [67]. The contribution of (GO@Si_3N_4) nanomaterials was also presented in Fig. 8 (b); the dielectric constant at 100 Hz frequency decreased when increasing the loading ratio of (Si_3N_4); this reduction may be attributed to a rise in polarity. This action agrees with previous studies [68–70].

Figure 9 (a) calculated the dielectric loss from Eq. (2S) in (SI). It exhibited elevated values at high frequencies, which significantly diminished as the frequency rose. This phenomenon can be attributed to improving the charge carriers' conductivity through the electric charge region. In addition to reducing the dielectric loss factor's magnitude. Furthermore, the electron energy is equivalent to the energy of the Fermi level. The dipoles caused the variation in the dielectric loss results with frequency. It attracts the energy from the electric field in the system to counteract the resistance of the surrounding dense materials through rotation. This absorbed energy reduces, or the amplitude's charge carriers transferred between the boundaries increase with increasing frequency. Therefore, the dipoles need higher energy in the system to achieve relaxation. In this case, the dielectric loss factor decreases [71].

A drop in the dielectric loss factor values was detected when the frequency increased for all nanocomposites. This is illustrated in Fig. 9(b), where the value at the same frequency rose with a rise in the concentration of Si_3N_4 nanoparticles in the polymer matrix, associated with the improved polarized diodes resulting from the surface [72].

A.C. electrical conductivity was considered by applying Eq. (3S) in (SI), and the result is presented in Fig. 10. at high frequencies, the conductivity increased with the increased frequency of the electrical field supplied, as presented in Fig. 10 (a). The observed rise in the findings can be attributed to the amplified charge polarization at higher frequencies and the movement of charge carriers. In addition, the presence of Si_3N_4 nanoparticles in the combined (GO@Si_3N_4) content increased the electronic polarization and the movement of charge carriers. This, in turn, results in an enhancement of the A.C. electrical conductivity, as exposed in Fig. 10 (b). The improved electrical conductivity of the nanocomposites is directly relative to the ratio of Si_3N_4 nanoparticles. This can be attributed to a growth in the number of ionic charge carriers and the development of

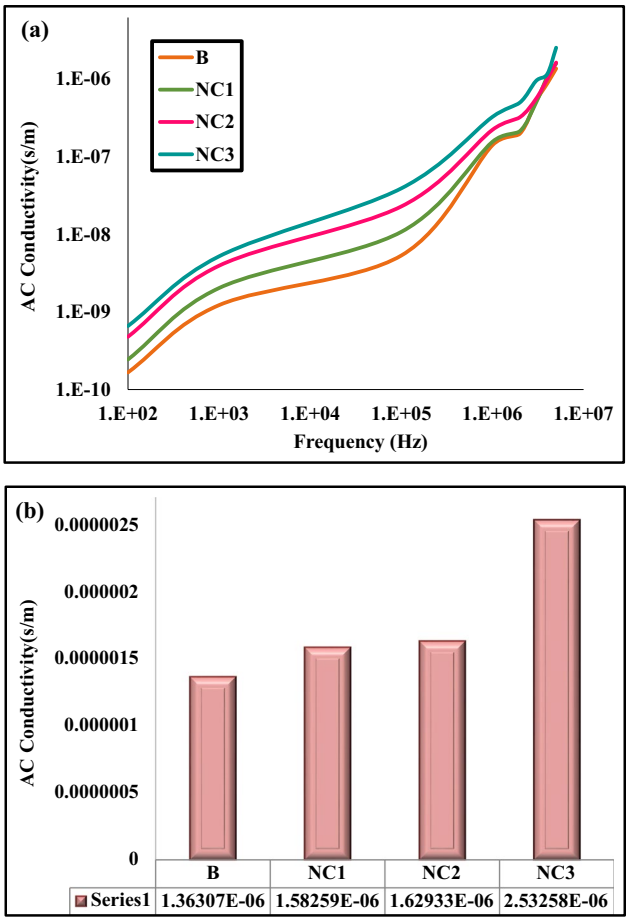

Fig. 10 Signifies A.C Electrical conductivity variation with (**a**) frequency and (**b**) Effect of (GO@Si_3N_4) content on AC electrical conductivity for (PEO-CMC-PANI/GO@Si_3N_4) nanocomposite at 5 MHz

a continuous network between GO and Si_3N_4 nanomaterials within the polymer matrix [59, 73, 74].

3.3 Gas Sensing Results of NO_2 Oxidizing Gas Vapors

The gas sensors were prepared by depositing the film on a substrate using the drop-casting technique and depositing aluminum electrodes with a mesh structure with a thickness (about 300 nm) on the sample's surface using thermal evaporation under vacuum conditions. The thermal evaporation process was carried out using an (Edward 306-Thermal Evaporation Coating Unit) system. The basin type was (Spiral Tungsten (w)). If the sedimentation was carried out under a vacuum or high sedimentation pressure of 10–5 mbar, The attainment of a high vacuum level was accomplished by utilizing rotary and diffusion pumps. The monitoring was conducted using Berani and Penning gauges. The two electrodes were linked with slender wires, and silver conductive paste was applied to them. Figure 11 (a) provides a diagram of the structures of gas sensors.

The gas sensor system comprises a stainless-steel cylindrical examination chamber, which consists of a 20 cm diameter and 10 cm height, then is evacuated by a rotary pump. The device features an entrance for the verified gas to enter and an air admittance valve to enable ambient air flow following evacuation. The chamber base is equipped with a multi-pin feed through, which allows the establishment of thermocouples, sensor electrodes, and electrical connections to the heater. A temperature controller type GEMO DT109 PID was utilized to control the temperature of the sensor's operation, and a thermocouple type (K) was placed within the chamber, which controlled a hot plate heater. A laptop computer is utilized to monitor

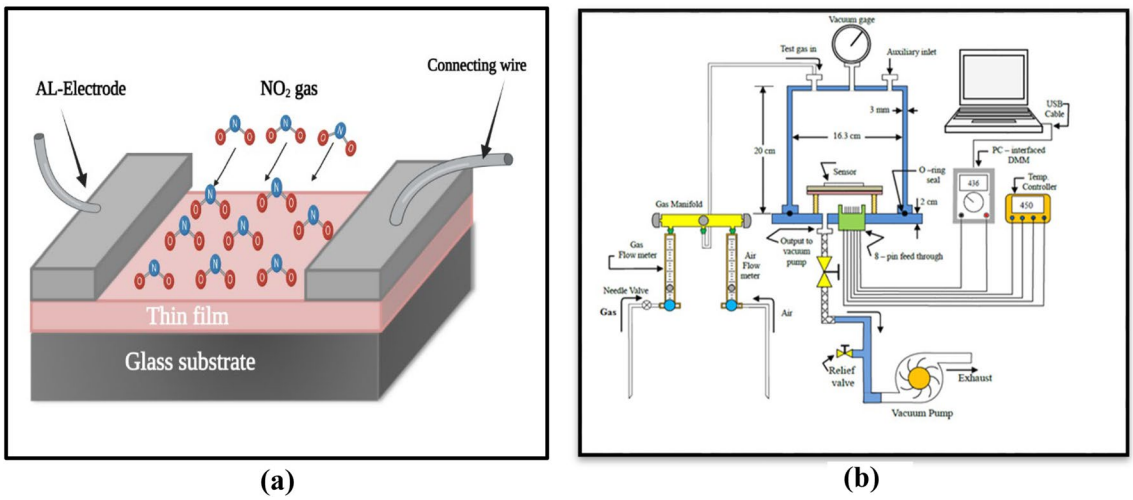

Fig. 11 The diagram of the (**a**) structures of gas sensors and (**b**) gas sensor system [75]

the sensor's resistance over time when it is exposed to the gas. A PC-interfaced digital multimeter of type Vector 70 C measures the resistance. The gas is circulated through a tube positioned above the sensor within the test chamber to ensure accurate sensitivity and quantify the changes in sensor resistance after exposure to a mixture of air and NO_2. This circulation is achieved using flow meters with the assistance of the arrangement of a needle valve. Figure 11 (b) displays the gas sensor system employed.

Figure 12 displays the behavior of the electrical resistance with open and closed gas vapor time utilizing the needle valves at three different operating temperatures (RT, 100 °C, and 200) °C. A 500 ppm is the constant concentration of NO_2 gas used in ambient air introduced into the testing chamber at each sample's ideal operating temperature. Before opening the gas, the resistance is continuously checked and eventually stabilizes over time. The gas is turned off after the resistance sharply rises to a stable level. Electrical resistance then went back to the original position. The nature of the interaction between the molecules of gas and the surface atoms of the detecting film considers the sensor's ability to detect the gas presence. The computer was used to measure the electrical resistance of all the samples. The measurements were taken using a digital multimeter called Vector 70C, connected to an interface. The nanofilms sensor, PEO-CMC-PANI/ GO@Si_3N_4, was produced and tested at various working temperatures.

The data in Fig. 13 of nanofilm sensors exhibit p-type semiconducting behavior due to the electrical resistance exhibiting a negative correlation with time. For example, electrical resistance decreased when oxidizing gas such as NO_2 was turned on, and resistance negatively correlated with time when the gas was turned on. It steadily increased, for instance, and recovered completely to its initial value after NO_2 gas was turned off because NO_2 is a chemical oxidant gas. When NO2 is present on the nanofilms sensor made of P-type semiconductors, it can receive electrons from the valence band, leading to a rise in the concentration of charge carriers known as holes. Consequently, the electrical conductivity increases while the electrical resistance decreases. The reduction in electrical resistance and improved electrical conductivity of the nanofilm sensors could be credited to the NO_2 adsorption onto the p-type semiconductors surfaces NC1, NC2, and NC3. The NO_2 acts as a chemical oxidant gas, leading to these changes in the sensors' properties. Consequently, the electrical resistance of every nanofilm-based sensor sample is reduced when exposed to NO_2 gas. It is evident that when exposed to an oxidizing gas, NO_2, the change in electrical resistance can be reversed entirely when exposed to a reducing gas like NH3. However, when NO_2 molecules were taken in, oxygen ions created a negatively charged NO2- species (chemical species) at the surface of the NC1, NC2, and NC3 nanofilms sensor. They are attached to the grain boundaries on the surface.

When a closed gas vapor is present, the electrical resistance initially increases. However, after the removal of NO_2, the resistance returns to its original value (Rair). This is because the NO_2- reacts with oxygen ions absorbed on the surface at the grain boundaries. This reaction leads to a decrease in the density of holes and a reduction in electrical conductivity, which causes a rise in electrical resistance; this behavior was similar to another study [76], they used carbon nanotubes, F-SWCNTs/ silver nanoparticles (AgNPs), and porous silicon (PSi) to detect the NO_2 gas as a sensor.

Figure 13 shows the improved electrical resistance of NO_2 gas with the increase in operating temperature. It was noticed that increasing the loading ratio of Si_3N_4 nanoparticles was an essential factor that affected the results.

Sensitivity (S%) (also often termed as the response) was calculated from Eq. (4S) in the (SI). According to results in Fig. 14 (a), (6.89%) was the highest sensitivity recorded to NO_2 at RT for the NC2 in a response time of (16 s) and recovery time of (19 s). The sensitivity is generally reduced as the temperature rises for the sample NC2. This indicates that the gas sensor does not require activation energy to interact with NO_2 gas and that the interaction is physical adsorption and polarity. This action agrees with previous studies [77]. However, for the NC1 and NC3 samples, the sensitivity increased with temperature at a specified range. This means that the gas sensor needs energy to activate the interaction with NO2 gas, and it has reached a high sensitivity. This behavior is similar to the following studies [78]; they fabricated carbon nanotubes (SWCNTs)/ silver nanoparticles (AgNPs) and porous silicon (PS).

The maximum sensitivity of NC1 of 3.64% was obtained at 200 °C, while the sensitivity of NC3 of 4.84% was obtained at 100 °C. When the operating temperature increased, a thermally activated procedure was induced that will lead to more substantial adsorption of gas species owing to the higher interaction of intense gas with the material's surface. It suggests enhanced chemical interactions at higher temperatures, possibly due to increased mobility of the NO_2 molecules that facilitate better adsorption on the sensor surfaces.

Sensitivity increased with increasing sample concentration, and gas sensitivity saturation was observed at about 5%. Increasing the nanoparticle concentration from 1 to 5% tends to stabilize or even increase the sensitivity at higher temperatures. It led to an increase in the chemisorbed NO_2, which in turn enhanced the desorption rates, hinting at the role of GO@Si_3N_4 in providing thermal stability and possibly active sites for NO_2 adsorption.

Nevertheless, when the concentration is extremely high, the enhancement in sensing ability may associated with the physical or chemical adsorption of NO_2, as shown in

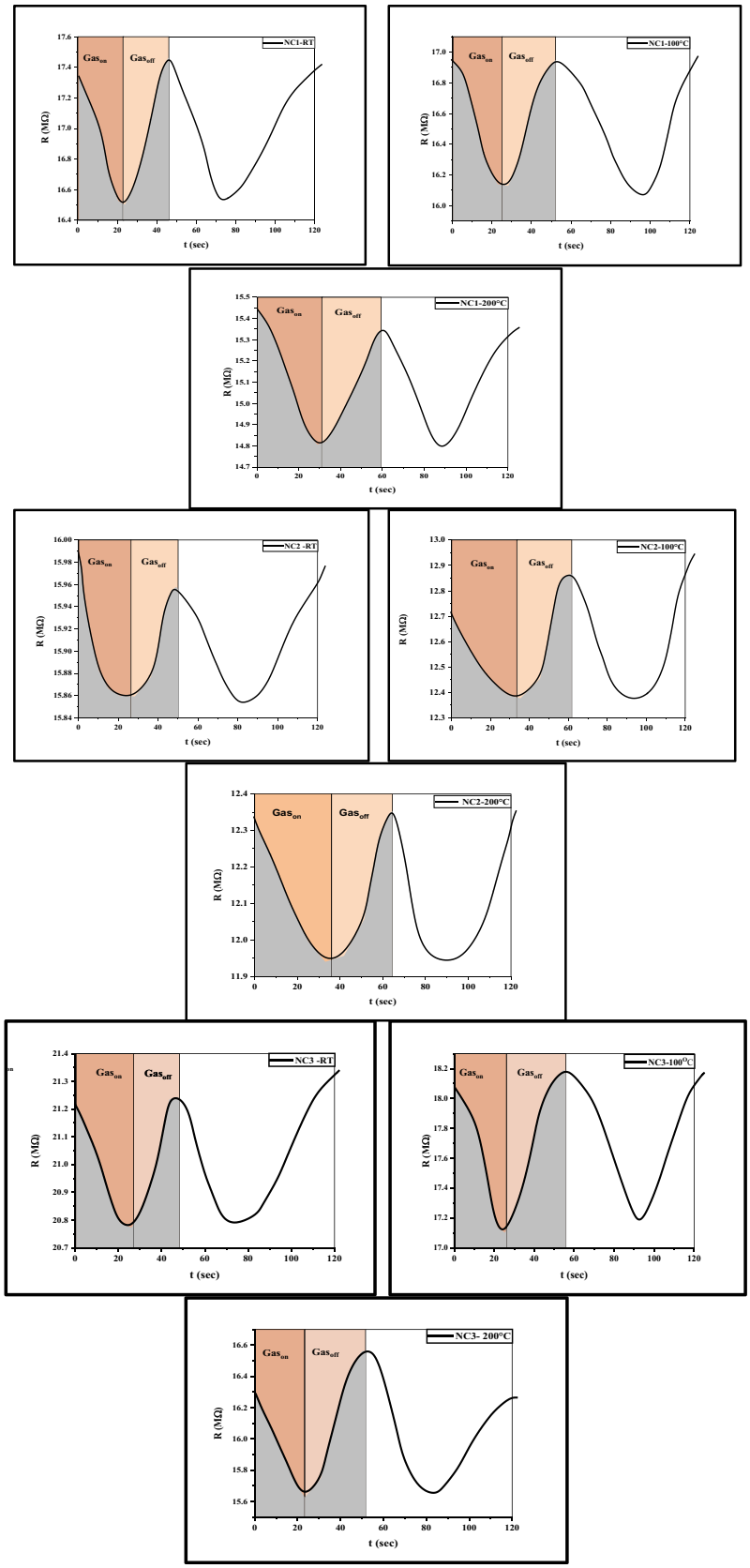

Fig. 12 The variation of resistance vs. time of NC1, NC2, and NC3 thin film sensors upon exposure to NO2 gas at different operating temperatures RT, 100, and 200 ^{O}C

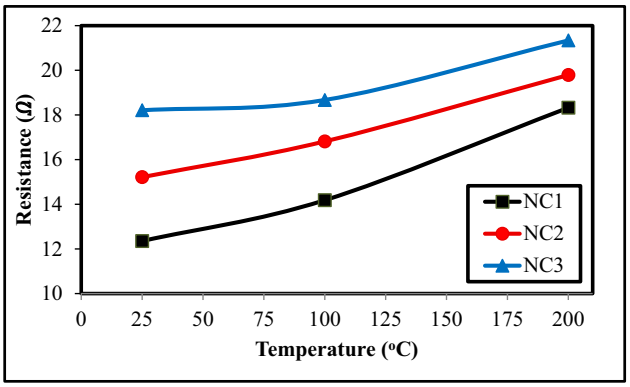

Fig. 13 The variation of resistance vs. operation temperature RT, 100 ^{0}C, and 200 ^{0}C thin film sensors upon exposure to NO_2 gas

Fig. 14 (b). This outcome is from the combined action of the acid–base doping or dedoping of PANI and the transfer of electrons between NO_2 molecules and GO. The functional group in GO and its high surface area facilitate the effortless passage of gas molecules. Furthermore, GO aspires to facilitate the creation of continuous sheets that would enhance the effective transfer of electricity between electrodes. Nitrogen dioxide (NO_2) exhibited potent oxidizing properties due to its great electron-withdrawing ability. Consequently, the electron transfer from the nanosheet surface of graphene oxide (GO) to nitrogen dioxide (NO_2) resulted in an increased concentration of positively charged holes and improved electrical conductivity in the GO. These variables facilitate the efficient adsorption of NO_2 onto the surface of GO (p-type).

The relationship between response and recovery time with three different operating temperatures is depicted in Table 3. This time, the quick response time (15 s) for the NC3 sample at ambient temperature for NO_2 gas is very short. It takes almost (37 s) to recover the sample resistance back to normal. The longest response time at RT for the NC3 sample could indicate that the gas sensor needs energy to activate the interaction with NO_2 gas. On the other hand, it illustrates how the recovery time for NO_2 test gas decreases with increasing operating temperature [77]. The quick recovery time was (16 s) for the NC2 sample at 200 °C for NO2 gas; the specific decreases with the surface reaction's activation energy and work function, potentially linked to an increase in vacancies. Improve the parameters for sensor operations. Recovery times vary inconsistently across the samples and temperatures, as depicted in Table 3. The recovery time is the time taken to return to the normal resistance when refreshed. The longest recovery time (37 s) at room temperature for the NC3 sample. This could indicate stronger or more stable adsorption characteristics at lower temperatures, which take longer to revert. Conversely, the increase in recovery time at 200 °C for the NC1 sample suggests possible changes in the sensor surface or chemical state that slow the desorption process.

The well-dispersed and porous structure of the PEO-CMC-PANI-doped GO@Si_3N_4 nanomaterials results from the optimum concentration and homogeneous distribution, contributing to its high surface area. The extensive surface area of PANI facilitates optimal gas adsorption and enhances its catalytic properties, resulting in heightened sensor response and reduced response and recovery time. The comparison of several nanocomposites for NO_2 sensing,

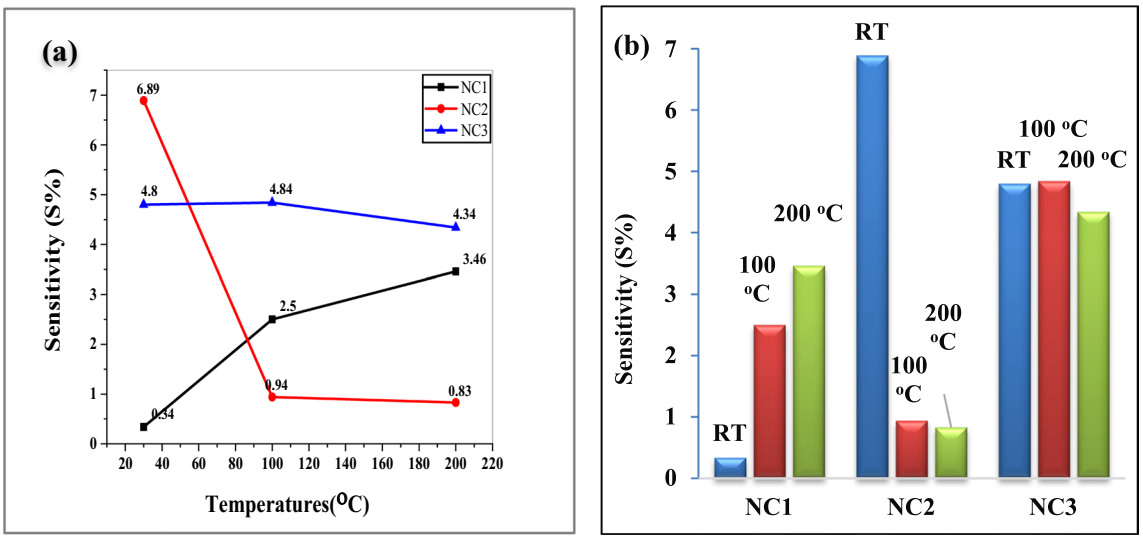

Fig. 14 Sensitivity (%) as a function at various operating temperatures RT, 100 ^{0}C, and 200 ^{0}C versus (**a**) temperature and (**b**) concentrations ratio of (NO2) gas vapor for NCs nanofilms sensor synthesized upon exposure to NO_2

Table 3 The response and recovery time for NC1, NC2, and NC3 nanofilm sensors at three different times, based on exposure to NO_2 gas

Sample	T (ºC)	Response time (sec)	Recovery time (sec)
NC1	RT	26	21
	100	24	16
	200	25	31
NC2	RT	16	19
	100	21	22
	200	27	21
NC3	RT	15	37
	100	19	17
	200	28	26

Table 4 Comparison of nanocomposite ability as NO_2 gas sensing from different literatures

Sensor material	Operating temperature (°C)	Target gas/vapor	Conc (ppm)	Sensor sensitivity (%)	Response time (sec)	Recovery time (sec)	Ref
Fe_2O_3-PANI	RT	NO_2	20	$2.29 * 10^2$	141	228	[79]
GO Al NPs–GO Pd NPs- GO	150	NO_2	1.2	1.44 2.89 0.46	5 min	30 min	[23]
Ni@ZnO/PANi	RT	NO_2	100	75%	82	399	[80]
rGO/ZnO–Au Nanoparticles	80 (60–90)	NO_2	100(20–100)	32.55	27	86	[81]
Graphene/SnO_2 Nanowires	150 (100–250)	NO_2	0.1 (0.01–0.1)	11	43	37	[82]
rGO/ZnO Nanoparticles	RT	NO_2	5 (1–25)	25.6%	165	499	[83]
In_2O_3/RGO–	RT	NO_2	30	8.25	4	24	[84]
PANI nanofibrous thin film	RT	NO_2	50	207.04	23	3	[85]
PEO–CMC–PANI/GO@Si_3N_4	RT-100–200	NO_2	500	6.86	16	19	Present work

as found in the literature, is shown in Table 4 alongside the results of our current study.

4 Conclusions

Fabricated new nanocomposites were successfully achieved using ternary blend polymers PEO-CMC-PANI reinforced by different concentrations of GO@Si_3N_4 nanomaterials. FE-SEM images showed the total surface change of samples a homogeneous surface. TEM micrographs of GO@Si_3N_4 show that the homogeneous dispersion of GO and Si3N4 were uniformly distributed and linked in most regions between GO and Si_3N_4 nanoparticles and nanocomposites. All samples generally showed strong absorption peaks of blended polymer and signs of nanomaterials crosslinked in the fabricated nanocomposites by FTIR. The XRD pattern of ternary blended polymers revealed the semi-crystalline of the matrix with shifting of the peaks after the contribution of nanomaterials without impact on the semicrystalline behavior. The dielectric constant improved from (15 to 20), where there was a decrease in the dielectric loss values with a rise in the frequency for all nanocomposites. AC electrical conductivity increases for (NCs) nanocomposites with the

rise in the concentration of GO@Si_3N_4. All the nanofilm sensors exhibit p-type semiconducting behavior. Electrical resistance decreases when oxidizing NO_2 gas is turned on. The resistance returned completely to its initial value (Rair) once the NO_2 gas was deactivated as a result of the reaction between NO_2 and oxygen ions absorbed on the surface at the grain boundaries. The electrical resistance of NO_2 gas exhibited a positive correlation with the operating temperature, reaching its peak at 200 °C. The NC2 sample exhibited the most incredible sensitivity to NO2 (6.89%) when operated at room temperature (RT), with a response time of 16 s and a recovery time of 19 s. The sensitivity generally decreases as the temperature increases for the sample NC2. However, for the NC1 and NC3 samples, the sensitivity increases with temperature at a specified range. Sensitivity increased with increasing sample concentration, and gas sensitivity saturation was observed at about 5%. The response time for NO_2 test gas increases as the operating temperature rises. This time, the quick response time (15 s) for the NC3 sample at ambient temperature for NO_2 gas is very short. It takes almost 37 s to recover the sample resistance back to normal, which is the longest response time at RT for the NC3 sample.

Supplementary Information The online version contains supplementary material available at https://doi.org/10.1007/s12633-024-03092-8.

Acknowledgements Rawaa A. Abdul-Nabi gratefully acknowledges the University of Babylon, College of Education for Pure Science, Iraq.

Author Contributions Rawaa A. Abdul-Nabi: Conceptualization, investigation, acquisition, software, formal analysis, data curation, writing – original draft and Funding. Ehssan Al-Bermany: Supervisor, validate, review, and edit, as well as manage project administration, investigation, and resources.

Funding None.

Data Availability No datasets were generated or analysed during the current study.

Declarations

Ethical Approval Not applicable.

Consent to Participate Not applicable.

Consent for Publication Not applicable.

Declaration of Generative AI in Scientific Writing Not applicable.

Competing Interests The authors declare no competing interests.

References

1. Lee DD (2001) Environmental gas sensors. IEEE Sens J 1:214–224. https://doi.org/10.1109/JSEN.2001.954834
2. Yunusa Z, Hamidon MN, Kaiser A et al (2014) Gas sensors: a review. SensorsTransducers 168:61–75
3. Jasim SA, Banimuslem HAJ, Alsultany FH et al (2023) Ammonia and nitrogen dioxide detection using ZnO/CNT nanocomposite synthesized by sol–gel technique. J Sol-Gel Sci Technol 108:734–741. https://doi.org/10.1007/s10971-023-06190-y
4. Padvi MN, Moholkar AV, Prasad SR, Prasad NR (2021) A critical review on design and development of gas sensing materials. Eng Sci 15:20–37. https://doi.org/10.30919/es8d431
5. Dobson PJ (2012) Nanosensors: physical, chemical, and biological, by Vinod Kumar Khanna. Contemp Phys 53:391–392. https://doi.org/10.1080/00107514.2012.689351
6. Naresh V, Lee N (2021) A review on biosensors and recent development of nanostructured materials-enabled biosensors. Sensors 21:1109. https://doi.org/10.3390/s21041109
7. Hulanicki A, Glab S, Ingman F (1991) Chemical sensors: definitions and classification. Pure Appl Chem 63:1247–1250. https://doi.org/10.1351/pac199163091247
8. Wahab R, Hwang IH, Shin HS et al (2012) Zinc oxide nanostructures and their applications. Intell Nanomater Process Prop Appl 3:183–212. https://doi.org/10.1002/9781118311974.ch5
9. Torsi L, Dodabalapur A, Sabbatini L, Zambonin P (2000) Multi-parameter gas sensors based on organic thin-film-transistors. Sensors Actuators B Chem 67:312–316. https://doi.org/10.1016/S0925-4005(00)00541-4
10. Wusiman M, Taghipour F (2022) Methods and mechanisms of gas sensor selectivity. Crit Rev Solid State Mater Sci 47:416–435. https://doi.org/10.1080/10408436.2021.1941752
11. Nikolic MV, Milovanovic V, Vasiljevic ZZ, Stamenkovic Z (2020) Semiconductor gas sensors: materials, technology, design, and application. Sensors (Switzerland) 20:1–31. https://doi.org/10.3390/s20226694
12. Mahmood L, Ghommem M, Bahroun Z (2023) Smart gas sensors: materials, technologies, practical applications, and use of machine learning – a review. J Appl Comput Mech 9:775–803. https://doi.org/10.22055/jacm.2023.41985.3851
13. Al-Bermany E, Chen B (2021) Preparation and characterisation of poly(ethylene glycol)-adsorbed graphene oxide nanosheets. Polym Int 70:341–351. https://doi.org/10.1002/pi.6140
14. Wang Y, Yu L, Sun Q, Xie F (2021) Hydroxypropyl methylcellulose and hydroxypropyl starch: rheological and gelation effects on the phase structure of their mixed hydrocolloid system. Food Hydrocoll 115:106598. https://doi.org/10.1016/j.foodhyd.2021.106598
15. Aldulaimi NR, Al-Bermany E, Al-Bermany E (2022) Tuning the bandgap and absorption behaviour of the newly-fabricated ultrahigh molecular weight polyethylene oxide- polyvinyl alcohol/graphene oxide hybrid nanocomposites. Polym Polym Compos 30:null. https://doi.org/10.1177/09673911221112196
16. Morsi MA, Oraby AH, Elshahawy AG, Abd El-Hady RM (2019) Preparation, structural analysis, morphological investigation and electrical properties of gold nanoparticles filled polyvinyl alcohol/carboxymethyl cellulose blend. J Mater Res Technol 8:5996–6010. https://doi.org/10.1016/j.jmrt.2019.09.074
17. Alsulami QA, Rajeh A (2021) Synthesis of the SWCNTs/TiO2 nanostructure and its effect study on the thermal, optical, and conductivity properties of the CMC/PEO blend. Results Phys 28. https://doi.org/10.1016/j.rinp.2021.104675
18. Hashim FS, Jabbar SA, Al-Bermany E, Abdali K (2024) Effect of inclusion ZnO-Co3O4 nanoparticles on the microstructural and optical properties of PVA-CMC polymeric blend for biomedical, UV shielding, and nuclear radiation shielding applications. Plasmonics. https://doi.org/10.1007/s11468-024-02379-1
19. Hameed TA, Mohamed F, Turky G, Salama A (2022) Carboxymethylcellulose/polyvinylpyrrolidone filled with Al-doped ZnO nanoparticles as a promising film for optoelectronic applications. Opt Mater (Amst) 134:1–7. https://doi.org/10.1016/j.optmat.2022.113097

20. Bai H, Shi G (2007) Gas sensors based on conducting polymers. Sensors 7:267–307. https://doi.org/10.3390/s7030267
21. Ansari R, Keivani MB (2006) Polyaniline conducting electroactive polymers thermal and environmental stability studies. E-J Chem 3:202–217. https://doi.org/10.1155/2006/395391
22. Pomfret SJ, Adams PN, Comfort NP, Monkman AP (1998) Inherently electrically conductive fibers wet spun from a sulfonic acid-doped polyaniline solution. Adv Mater 10:1351–1353. https://doi.org/10.1002/(SICI)1521-4095(199811)10:16%3c1351::AID-ADMA1351%3e3.0.CO;2-8
23. Cho B, Yoon J, Hahm MG et al (2014) Graphene-based gas sensor: metal decoration effect and application to a flexible device. J Mater Chem C 2:5280–5285. https://doi.org/10.1039/C4TC00510D
24. Gupta Chatterjee S, Chatterjee S, Ray AK, Chakraborty AK (2015) Graphene-metal oxide nanohybrids for toxic gas sensor: a review. Sensors Actuators B Chem 221:1170–1181. https://doi.org/10.1016/j.snb.2015.07.070
25. Schedin F, Geim AK, Morozov SV et al (2007) Detection of individual gas molecules adsorbed on graphene. Nat Mater 6:652–655. https://doi.org/10.1038/nmat1967
26. Al-shammari AK, Al-Bermany E (2022) Polymer functional group impact on the thermo-mechanical properties of polyacrylic acid, polyacrylic amide-poly (vinyl alcohol) nanocomposites reinforced by graphene oxide nanosheets. J Polym Res 29:1–12
27. Novoselov KS, Geim AK, Morozov SV et al (2004) Electric Field Effect in Atomically Thin Carbon Films. Science (80-) 306:666–669. https://doi.org/10.1126/science.1102896
28. Ghazi RA, Al-Mayalee KH, Al-Bermany E et al (2022) Impact of polymer molecular weights and graphene nanosheets on fabricated PVA-PEG/GO nanocomposites: morphology, sorption behavior and shielding application. AIMS Mater Sci 9:584–603. https://doi.org/10.3934/matersci.2022035
29. Al-Bermany E, Qais D, Al-Rubaye S (2019) Graphene effect on the mechanical properties of poly (ethylene oxide)/ graphene oxide nanocomposites using ultrasound technique. J Phys Conf Ser 1234:012011. https://doi.org/10.1088/1742-6596/1234/1/012011
30. Radadiya TMM, Radadiya TMM, Radadiva TM et al (2015) A properties of graphene. Eur J Mater Sci 2:6–18
31. Al-Abbas SS, Ghazi RA, Al-shammari AK et al (2021) Influence of the polymer molecular weights on the electrical properties of Poly(vinyl alcohol) – Poly(ethylene glycols)/Graphene oxide nanocomposites. Mater Today Proc 42:2469–2474. https://doi.org/10.1016/j.matpr.2020.12.565
32. Kadhim MA, Al-Bermany E (2020) Enhance the electrical properties of the novel fabricated pmma-pva/ graphene based nanocomposites. J Green Eng 10:3465–3483
33. Huang J, Huang Z, Yi S et al (2013) Fe-catalyzed growth of one-dimensional α-Si3N4 nanostructures and their cathodoluminescence properties. Sci Rep 3:1–9. https://doi.org/10.1038/srep03504
34. Chandra Mishra A, Sharma AK, Lohia P, Dwivedi DK (2024) Silicon nitride (Si3N4) leads to enhanced performance of silica-silver based plasmonic sensor for colorectal cancer detection under optimum radiation damping. Solid State Commun 387:115533. https://doi.org/10.1016/j.ssc.2024.115533
35. Sylenko PM, Shlapak AM, Petrovska SS et al (2015) Direct nitridation synthesis and characterization of Si3N4 nanofibers. Res Chem Intermed 41:10037–10048. https://doi.org/10.1007/s11164-015-2011-8
36. Chen Z, Wang J, Wang Y (2021) Strategies for the performance enhancement of graphene-based gas sensors: a review. Talanta 235:122745. https://doi.org/10.1016/j.talanta.2021.122745
37. Niu F, Liu JM, Tao LM et al (2013) Nitrogen and silica co-doped graphene nanosheets for NO2 gas sensing. J Mater Chem A 1:6130–6133. https://doi.org/10.1039/c3ta11070b
38. Gutés A, Hsia B, Sussman A et al (2012) Graphene decoration with metal nanoparticles: towards easy integration for sensing applications. Nanoscale 4:438–440. https://doi.org/10.1039/C1NR11537E
39. Pumera M, Ambrosi A, Bonanni A et al (2010) Graphene for electrochemical sensing and biosensing. TrAC Trends Anal Chem 29:954–965. https://doi.org/10.1016/j.trac.2010.05.011
40 Al-Bermany E, Chen B (2023) Effect of the functional groups of polymers on their adsorption behavior on graphene oxide nanosheets. Macromol Chem Phys 224:null. https://doi.org/10.1002/macp.202300101
41. Arya A, Saykar NG, Sharma AL (2019) Impact of shape (nanofiller vs. nanorod) of TiO 2 nanoparticle on free-standing solid polymeric separator for energy storage/conversion devices. J Appl Polym Sci 136. https://doi.org/10.1002/app.47361
42 Aldulaimi NR, Al-Bermany E (2021) New fabricated UHMWPEO-PVA hybrid nanocomposites reinforced by GO nanosheets: structure and DC electrical behaviour. J Phys Conf Ser 1973:null. https://doi.org/10.1088/1742-6596/1973/1/012164
43. Lin Q, Chang J, Gao M, Ma H (2017) Synthesis of magnetic epichlorohydrin cross-linked carboxymethyl cellulose microspheres and their adsorption behavior for methylene blue. J Environ Sci Heal Part A 52:106–116. https://doi.org/10.1080/10934529.2016.1237117
44. Thakur AK, Choudhary RB, Majumder M, Majhi M (2018) Fairly improved pseudocapacitance of PTP/PANI/TiO2 nanohybrid composite electrode material for supercapacitor applications. Ionics (Kiel) 24:257–268. https://doi.org/10.1007/s11581-017-2183-x
45. Khasim S (2019) Polyaniline-Graphene nanoplatelet composite films with improved conductivity for high performance X-band microwave shielding applications. Results Phys 12:1073–1081. https://doi.org/10.1016/j.rinp.2018.12.087
46. Sirota V, Lukianova O, Krasilnikov V et al (2016) Microstructural and physical properties of magnesium oxide-doped silicon nitride ceramics. Results Phys 6:82–83. https://doi.org/10.1016/j.rinp.2016.01.005
47. Rathi K, Pal K (2017) Impact of doping on GO: fast response-recovery humidity sensor. ACS Omega 2:842–851. https://doi.org/10.1021/acsomega.6b00399
48. Moussa I, Khiari R, Moussa A et al (2019) Preparation and characterization of carboxymethyl cellulose with a high degree of substitution from agricultural wastes. Fibers Polym 20:933–943. https://doi.org/10.1007/s12221-019-8665-x
49. Maile NC, Shinde SK, Patil KS et al (2019) Capacitive property studies of inexpensive SILAR synthesized polyaniline thin films for supercapacitor application. SN Appl Sci 1:1333. https://doi.org/10.1007/s42452-019-1403-6
50. Alawi AI, Al-Bermany E, Alnayli RS et al (2024) Impact of SiO2–GO hybrid nanomaterials on opto-electronic behavior for novel glass quinary (PAAm–PVP–PVA/SiO2–GO) hybrid nanocomposite for antibacterial activity and shielding applications. Opt Quantum Electron 56:429. https://doi.org/10.1007/s11082-023-06070-3
51. Diaham S, Saysouk F, Locatelli M (2017) Improvement of the electrical properties of polyimide films with silicon nitride nanoparticles. In: 2017 IEEE 12th Nanotechnology Materials and Devices Conference (NMDC). IEEE, pp 60–61. https://doi.org/10.1109/NMDC.2017.8350503
52. Shokry A, Khalil MMA, Ibrahim H et al (2019) Highly luminescent ternary nanocomposite of polyaniline, silver nanoparticles and graphene oxide quantum dots. Sci Rep 9:16984. https://doi.org/10.1038/s41598-019-53584-6

53. Yuk JS, Jin J-H, Alocilja EC, Rose JB (2009) Performance enhancement of polyaniline-based polymeric wire biosensor. Biosens Bioelectron 24:1348–1352. https://doi.org/10.1016/j.bios.2008.07.079
54. Miao J, Li H, Qiu H et al (2018) Graphene/PANI hybrid film with enhanced thermal conductivity by in situ polymerization. J Mater Sci 53:8855–8865. https://doi.org/10.1007/s10853-018-2112-z
55. Abdelrazek EM, Elashmawi IS, El-khodary A, Yassin A (2010) Structural, optical, thermal and electrical studies on PVA/PVP blends filled with lithium bromide. Curr Appl Phys 10:607–613. https://doi.org/10.1016/j.cap.2009.08.005
56. Wu S, Guo J, Wang Y et al (2021) Facile preparation of magnetic sodium alginate/carboxymethyl cellulose composite hydrogel for removal of heavy metal ions from aqueous solution. J Mater Sci 56:13096–13107. https://doi.org/10.1007/s10853-021-06044-4
57. Khurana S, Chandra A (2018) Ionic liquid-based organic–inorganic hybrid electrolytes: impact of in situ obtained and dispersed silica. J Polym Sci Part B Polym Phys 56:207–218. https://doi.org/10.1002/polb.24533
58. Zhang M, Zhang A, Li Q et al (2019) Conductivity of PEO/PLA doped liquid crystal ionomer solid polymer electrolyte in mesomorphic range. J Polym Environ 27:2369–2379. https://doi.org/10.1007/s10924-019-01521-z
59. Abdali K, Abass KH, Al-Bermany E et al (2022) Morphological, optical, electrical characterizations and Anti- Escherichia coli Bacterial Efficiency (AECBE) of PVA/PAAm/PEO polymer blend doped with silver NPs. Nano Biomed Eng 14:114–122. https://doi.org/10.5101/nbe.v14i2.p114-122
60. Jhansirani K, Dubey RS, More MA, Singh S (2016) Deposition of silicon nitride films using chemical vapor deposition for photovoltaic applications. Results Phys 6:1059–1063. https://doi.org/10.1016/j.rinp.2016.11.029
61. Al-Bermany E, Mekhalif AT, Banimuslem HA et al (2023) Effect of green synthesis bimetallic Ag@SiO2 core–shell nanoparticles on absorption behavior and electrical properties of PVA-PEO nanocomposites for optoelectronic applications. Silicon 15:4095–4107. https://doi.org/10.1007/s12633-023-02332-7
62. Deshmukh SP, Dhodamani AG, Patil SM et al (2020) Interfacially interactive ternary silver-supported polyaniline/multiwalled carbon nanotube nanocomposites for catalytic and antibacterial activity. ACS Omega 5:219–227. https://doi.org/10.1021/acsomega.9b02526
63. Zhu S-F, Li Z-C, Zhao X-H et al (2016) The green synthesis and characterization of carboxymethyl cellulose medical dressing with silver nanoparticles. In: Proceedings of the 2016 3rd International Conference on Mechatronics and Information Technology. Atlantis Press, Paris, pp 420–425
64. Abdel-Galil A, Ali HE, Atta A, Balboul MR (2014) Influence of nanostructured TiO2 additives on some physical characteristics of carboxymethyl cellulose (CMC). J Radiat Res Appl Sci 7:36–43. https://doi.org/10.1016/j.jrras.2013.11.004
65. Al-shammari AK, Al-Bermany E, Al-Bermany E (2021) New fabricated (PAA-PVA/GO) and (PAAm-PVA/GO) nanocomposites: functional groups and graphene nanosheets effect on the morphology and mechanical properties. J Phys Conf Ser 1973:null. https://doi.org/10.1088/1742-6596/1973/1/012165
66. El Fewaty NH, El Sayed AM, Hafez RS (2016) Synthesis, structural and optical properties of tin oxide nanoparticles and its CMC/PEG–PVA nanocomposite films. Polym Sci Ser A 58:1004–1016. https://doi.org/10.1134/S0965545X16060055
67. Hassan JMKA (2015) Effect of SiC particles on dielectrically properties of epoxy reinforcement by (Bi-Directional) glass fiber. J Mater Sci Eng 04:3–5. https://doi.org/10.4172/2169-0022.1000168
68. Alawi AI, Al-Bermany E (2023) Newly fabricated ternary PAAm-PVA-PVP blend polymer doped by SiO2: absorption and dielectric characteristics for solar cell applications and antibacterial activity. Silicon 15:5773–5789. https://doi.org/10.1007/s12633-023-02477-5
69. McLachlan DS, Chiteme C, Park C et al (2005) AC and DC percolative conductivity of single wall carbon nanotube polymer composites. J Polym Sci Part B Polym Phys 43:3273–3287. https://doi.org/10.1002/polb.20597
70 Ali NA, Noori FTM, Hussin SI (2010) Dielectric properties of industrial polymer composite materials. J Al-Nahrain Univ Sci 13:73–77. https://doi.org/10.22401/JNUS.13.1.10
71. Arun Prakash VR, Rajadurai A (2016) Mechanical, thermal and dielectric characterization of iron oxide particles dispersed glass fiber epoxy resin hybrid composite. Dig J Nanomater Biostruct 11:373–380
72. Jabbar SA, Khalil SM, Abdulridha AR et al (2022) Dielectric, AC conductivity and optical characterizations of (PVA-PEG) doped sro hybrid nanocomposites. Key Eng Mater 936:83–92. https://doi.org/10.4028/p-41a757
73. Ju S, Chen M, Zhang H, Zhang Z (2014) Dielectric properties of nanosilica/low-density polyethylene composites: the surface chemistry of nanoparticles and deep traps induced by nanoparticles. Express Polym Lett 8:682–691. https://doi.org/10.3144/expresspolymlett.2014.71
74. Abdullah OG, Jamal GM, Tahir DA, Saeed SR (2011) Electrical characterization of polyester reinforced by carbon black particles. Int J Appl Phys Math 1:101–105. https://doi.org/10.7763/IJAPM.2011.V1.20
75. Abdul Wahid KI, Chaker C, Chaker H (2023) Ni-doped SnO2 thin films for NO2 gas sensing application. Sensors Actuators A Phys 360:114498. https://doi.org/10.1016/j.sna.2023.114498
76. Mahmood WK, Naje AN (2018) Fabrication of room temperature NO2 gas sensor based on silver nanoparticles-decorated carbon nanotubes. J Nano- Electron Phys 10:05020-1–05020-6. https://doi.org/10.21272/jnep.10(5).05020
77. Mahmood WK, Rashid TM, Rahmah MI et al (2024) Empowering NO2 detection: synthesis of highly responsive Au/Cu-doped iron oxide nanoparticles as gas sensors through laser ablation. Plasmonics. https://doi.org/10.1007/s11468-024-02235-2
78. Naje AN, Mahmood WK (2018) Sensitivity performance of single wall carbon nanotubes gas sensor on silicon and porous silicon. IOP Conf Ser Mater Sci Eng 454:012070. https://doi.org/10.1088/1757-899X/454/1/012070
79. Sonker RK, Yadav BC (2017) Development of Fe 2 O 3 –PANI nanocomposite thin film based sensor for NO 2 detection. J Taiwan Inst Chem Eng 77:276–281. https://doi.org/10.1016/j.jtice.2017.04.042
80. Jain S, Karmakar N, Shah A, Shimpi NG (2019) Development of Ni doped ZnO/polyaniline nanocomposites as high response room temperature NO2 sensor. Mater Sci Eng B 247:114381. https://doi.org/10.1016/j.mseb.2019.114381
81. Tung TT, Chien NV, Van Duy N et al (2019) Magnetic iron oxide nanoparticles decorated graphene for chemoresistive gas sensing: the particle size effects. J Colloid Interface Sci 539:315–325. https://doi.org/10.1016/j.jcis.2018.12.077
82. Van Quang V, Van Dung N, Sy Trong N et al (2014) Outstanding gas-sensing performance of graphene/SnO2 nanowire Schottky junctions. Appl Phys Lett 105:13107. https://doi.org/10.1063/1.4887486
83. Liu S, Yu B, Zhang H et al (2014) Enhancing NO2 gas sensing performances at room temperature based on reduced graphene oxide-ZnO nanoparticles hybrids. Sensors Actuators B Chem 202:272–278. https://doi.org/10.1016/j.snb.2014.05.086

84. Gu F, Nie R, Han D, Wang Z (2015) In2O3–graphene nanocomposite based gas sensor for selective detection of NO2 at room temperature. Sensors Actuators B Chem 219:94–99. https://doi.org/10.1016/j.snb.2015.04.119
85. Xie D, Jiang Y, Pan W et al (2002) Fabrication and characterization of polyaniline-based gas sensor by ultra-thin film technology. Sensors Actuators B Chem 81:158–164. https://doi.org/10.1016/S0925-4005(01)00946-7

Terms and Conditions

Springer Nature journal content, brought to you courtesy of Springer Nature Customer Service Center GmbH (“Springer Nature”).
Springer Nature supports a reasonable amount of sharing of research papers by authors, subscribers and authorised users (“Users”), for small-scale personal, non-commercial use provided that all copyright, trade and service marks and other proprietary notices are maintained. By accessing, sharing, receiving or otherwise using the Springer Nature journal content you agree to these terms of use (“Terms”). For these purposes, Springer Nature considers academic use (by researchers and students) to be non-commercial.
These Terms are supplementary and will apply in addition to any applicable website terms and conditions, a relevant site licence or a personal subscription. These Terms will prevail over any conflict or ambiguity with regards to the relevant terms, a site licence or a personal subscription (to the extent of the conflict or ambiguity only). For Creative Commons-licensed articles, the terms of the Creative Commons license used will apply.
We collect and use personal data to provide access to the Springer Nature journal content. We may also use these personal data internally within ResearchGate and Springer Nature and as agreed share it, in an anonymised way, for purposes of tracking, analysis and reporting. We will not otherwise disclose your personal data outside the ResearchGate or the Springer Nature group of companies unless we have your permission as detailed in the Privacy Policy.
While Users may use the Springer Nature journal content for small scale, personal non-commercial use, it is important to note that Users may not:

1. use such content for the purpose of providing other users with access on a regular or large scale basis or as a means to circumvent access control;
2. use such content where to do so would be considered a criminal or statutory offence in any jurisdiction, or gives rise to civil liability, or is otherwise unlawful;
3. falsely or misleadingly imply or suggest endorsement, approval , sponsorship, or association unless explicitly agreed to by Springer Nature in writing;
4. use bots or other automated methods to access the content or redirect messages
5. override any security feature or exclusionary protocol; or
6. share the content in order to create substitute for Springer Nature products or services or a systematic database of Springer Nature journal content.

In line with the restriction against commercial use, Springer Nature does not permit the creation of a product or service that creates revenue, royalties, rent or income from our content or its inclusion as part of a paid for service or for other commercial gain. Springer Nature journal content cannot be used for inter-library loans and librarians may not upload Springer Nature journal content on a large scale into their, or any other, institutional repository.
These terms of use are reviewed regularly and may be amended at any time. Springer Nature is not obligated to publish any information or content on this website and may remove it or features or functionality at our sole discretion, at any time with or without notice. Springer Nature may revoke this licence to you at any time and remove access to any copies of the Springer Nature journal content which have been saved.
To the fullest extent permitted by law, Springer Nature makes no warranties, representations or guarantees to Users, either express or implied with respect to the Springer nature journal content and all parties disclaim and waive any implied warranties or warranties imposed by law, including merchantability or fitness for any particular purpose.
Please note that these rights do not automatically extend to content, data or other material published by Springer Nature that may be licensed from third parties.
If you would like to use or distribute our Springer Nature journal content to a wider audience or on a regular basis or in any other manner not expressly permitted by these Terms, please contact Springer Nature at

onlineservice@springernature.com